Microgravity Sci. Technol. (2014) 26:89–99
DOI 10.1007/s12217-014-9377-x

ORIGINAL ARTICLE

ISS Droplet Combustion Experiments - Uncertainties in Droplet Sizes and Burning Rates

Benjamin D. Shaw

Received: 29 October 2013 / Accepted: 4 June 2014 / Published online: 19 June 2014

Abstract Methodologies are developed for evaluating uncertainties in droplet size measurements and burning rates for droplet combustion experiments that have been performed on the International Space Station. Different uncertainty sources are considered and propagated into the combined standard uncertainties via the Taylor series method. The local polynomial method is used to provide estimates of instantaneous burning rates. Results from analyses of non-sooting (methanol) or lightly sooting (heptane) droplets as well as moderately sooting (decane/propylbenzene) droplets are presented. Ninety-five percent expanded uncertainties in droplet diameters and burning rates are typically about 0.1 mm and 0.005 mm^2/s, respectively, for methanol and heptane droplets and 0.1 mm and 0.02 mm^2/s for decane/propylbenzene droplets, though uncertainties can be larger during ignition and extinction events.

Keywords Droplet · Combustion · International space station · Uncertainty

Nomenclature

A_d	projected area of a droplet
A_p	area of an individual pixel
b_Γ	type B standard uncertainty for the generic quantity Γ
$b_{Y_i Y_j}$	covariance terms in Eq. (27)
d	equivalent droplet diameter
E	variable defined in Eq. (3)
G	kernel in Eq. (3)
h	bandwidth
H	height of the camera field of view
k	coverage factor
K	droplet burning rate (= -dY/dt = - $d(d^2)/dt$)
n	total number of points in a data set
N	total number of camera pixels
N_{p_i}	number of pixels comprising a droplet image
p	polynomial order
s_Γ	type A standard uncertainty for the generic quantity Γ
$s_{Y_i Y_j}$	covariance terms in Eq. (28)
t	time
u_Γ	combined standard uncertainty for the generic quantity Γ
U_Γ	expanded uncertainty for the generic quantity Γ
W	width of the camera field of view
[W]	matrix defined after Eq. (6)
[X]	matrix defined after Eq. (6)
Y	square of the equivalent droplet diameter
[Y]	column vector defined after Eq. (6)
[Z]	matrix defined by Eq. (6)
β_j	fitting coefficient in Eq. (3)
$\hat{\beta}$	optimized fitting coefficient
δN_{p_i}	the number of pixels in a strip of thickness φ_i that bounds the droplet edge
φ_i	the thickness of a strip of pixels that bounds the droplet edge

Subscripts

i	image "i" or matrix element
gd	grayscale discretization
Γ	generic variable

B. D. Shaw (✉)
University of California, Davis, CA 95616 USA
e-mail: bdshaw@ucdavis.edu

j summation index or matrix element
sd spatial discretization

Introduction

This research is in support of two experiment campaigns performed onboard the International Space Station (ISS), the Droplet Flame Extinguishment in Microgravity (FLEX) and the Fundamental Studies in Droplet Combustion and Flame Extinguishment in Microgravity (FLEX-2) experiments. The FLEX and FLEX-2 research efforts use reduced-gravity droplet combustion, with the resulting simplified (nominally spherical) geometry, to investigate flammability and extinction under conditions relevant to space exploration as well as fundamental aspects of condensed-phase combustion of fuels. These experiments are designed to provide high-fidelity results under tightly controlled conditions that can, for example, be used to validate both detailed and simplified combustion models. Data of critical importance from these experiments include time variations in droplet diameters as well as the negative of the rate that the square of the droplet diameter decreases with time (the so-called burning rate). Accurate measurements of the droplet diameter can enable comparison with theories that relate the moment of flame extinction to the instantaneous droplet size (Law 1975; Zhang et al. 1996; Farouk and Dryer 2012). Other phenomena that depend on the instantaneous droplet diameter are the flame diameter and the importance of radiant heat losses from the flame zone (Marchese and Dryer 1997).

Various analytical and computational models have been proposed to predict droplet burning rates (Marchese and Dryer 1997; Williams 1985; Sirignano 2010; Law 2006). These models may be employed for different purposes, e.g., for modeling combustion of slowly moving individual droplets in a spray flame, for evaluation of chemical kinetic data to predict flame extinction, or to provide fundamental information on reduced-gravity combustion in the presence of flame suppressants. Such models will ideally be assessed by comparison with accurate experimental data such as from the FLEX and FLEX-2 experiments or drop tower experiments (e.g., Farouk et al. 2013; Liu et al. 2013) enabling the models to provide reliable predictions under situations where accurate experimental data do not exist. However, uncertainties that are associated with the experimental data need to be assessed so that merits of the models can be determined in a rational manner.

The focus of the present manuscript is to develop and present methodologies that can be employed for calculating uncertainty estimates of droplet sizes and burning rates obtained from the ISS experiments. These methodologies are also used here for analyses of representative FLEX and FLEX-2 data sets. The data that are evaluated here were

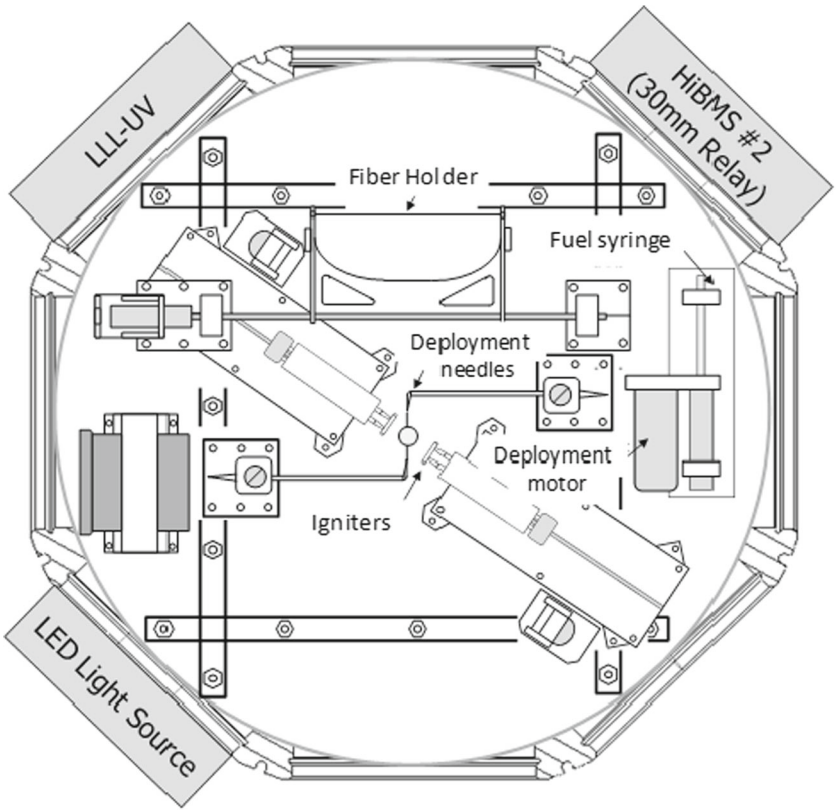

Fig. 1 Schematic of the Multi-user Droplet Combustion Apparatus (MDCA)

obtained from a previous NASA analysis (Dietrich et al. 2013). The data in (Dietrich et al. 2013) do not include detailed estimates of uncertainties.

The work described here will first use the local polynomial method (Fan and Gubels 1995) to provide curve fits for the square of the droplet diameter vs. time. We will then demonstrate how these curve fits can be used for evaluation of local (instantaneous) burning rates. We will then evaluate uncertainties for droplet sizes and burning rates for FLEX and FLEX-2 data sets for droplets composed of three different fuels, i.e., methanol, n-heptane, and a decane/propylbenzene mixture.

Backlit Droplet Images

In both the FLEX and FLEX-2 experiments, droplets were burned within the Multiuser Droplet Combustion Apparatus (MDCA) that has been installed on the ISS. This facility (Fig. 1) (Dietrich et al. 2013) allows for combustion of either free floating or fiber-supported (tethered) droplets inside of a pressure chamber. Initial droplet diameters are generally in the range 2 – 6 mm. The gas composition and pressure inside the chamber are controlled and droplets of different initial compositions can be burned. The MDCA facility allows measurements of droplets and flames via imaging, soot volume fractions via laser extinction, radiation emitted from flames via radiometers, as well as chamber temperatures, pressures and compositions. More detailed descriptions of the experimental apparatus are available (Dietrich et al. 2013).

The images used for droplet sizing are produced by collimating the light from a fiber-coupled light emitting diode (LED) and then directing this light past a droplet and into a telecentric lens. This lens directs the light into a monochrome digital camera (1024 x 1024 pixels). The collimated light and telecentric lens combination ideally produces well-defined shadows of objects on the camera image sensor array. Similar types of systems are used in machine vision applications (Webster 1999).

Representative backlit droplet images are shown in Fig. 2. The droplet in Fig. 2a is a fiber-supported (tethered) methanol droplet while a free (unsupported) heptane droplet is shown in Fig. 2b. Agglomerated soot formed during combustion of this heptane droplet is also evident as the small dark particles located several radii from the droplet center. Figure 2c shows an unsupported decane/propylbenzene droplet (initially 50% decane by volume). This is a moderately-sooting fuel combination, with large soot agglomerates visible. These agglomerates can make it difficult to determine the droplet size, e.g., by obscuring the edge, which increases uncertainties in the measurements. Dembia et al. (2012) have developed a methodology for addressing this issue, though we do not evaluate uncertainties associated with the approach of Dembia et al. (2012).

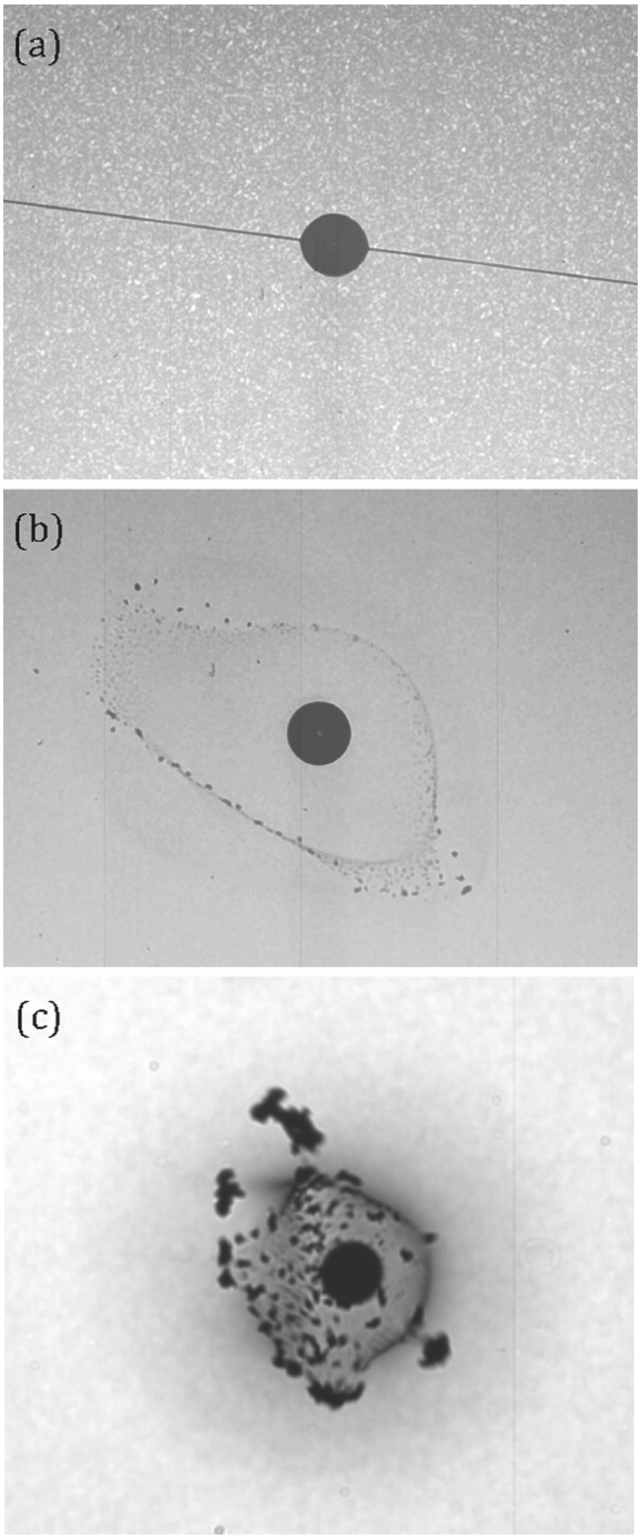

Fig. 2 Representative backlit images of burning droplets: **a** methanol; **b** heptane; and **c** decane/propylbenzene

Evaluation of Droplet Sizes and Burning Rates

For the purposes of this manuscript, we employ droplet size data that were previously obtained by manually specifying grayscale values for the edge pixels during a digital image analysis (Dietrich et al. 2013). In Dietrich et al. (2013), once the droplet edge has been specified, the projected area of the droplet, A_d, is determined by summing the areas of all pixels contained within the droplet boundary. The square of the droplet diameter is calculated using the projected area of the droplet, A_d, which is the blocked region of the collimated beam from the backlight (the "droplet shadow"). The shadow area is determined as the number of pixels, N_p, within the droplet shadow multiplied by the area of an individual pixel, A_p. The variable A_p is determined via calibration of the imaging system, e.g., by dividing the length and width of the field of view by the number of pixels. This yields Eq. (1) for the square of the diameter, d, of an equivalent droplet.

$$d^2 = \frac{4N_p A_p}{\pi} \tag{1}$$

Uncertainties in d^2 thus are determined by the uncertainties in N_p and A_p. By letting $Y_i = d_i^2$, where the subscript i refers to image i, we can write Eq. (2). The variable Y is employed to simplify later formulae.

$$Y_i = \frac{4N_{p_i} A_p}{\pi} \tag{2}$$

For estimates of burning rates (K) as well as estimates of uncertainties in Y and K, the method of local polynomial fitting (Fan and Gubels 1995) was used. The local polynomial method minimizes the objective function shown in Eq. (3), i.e., E, which represents a weighted squared error at a particular time t, is minimized.

$$E = \sum_{i=1}^{n} \left[\left(Y_i - \sum_{j=0}^{p} \beta_j \, (t_i - t)^j \right)^2 G\left(\frac{t_i - t}{h} \right) \right] \tag{3}$$

Here, n is the total number of data points, t is the particular point in time where the fit is being applied, p is the order of the polynomial (we used p = 2, as discussed later), G is the kernel, and h is the bandwidth. Equation (3) is minimized by finding appropriate (optimized) values for the coefficients β_0, β_1, β_2, ... For these analyses a Gaussian kernel was used. The bandwidth h is an adjustable parameter that essentially allows for multiresolution analysis. Small values of h will cause the fit to more closely follow fluctuations in the data while increasing h will smooth the fit by filtering out shorter timescale fluctuations in the data. It is noted that Liu et al. (2013) have used polynomials of various orders to evaluate burning rates of droplets, they did not evaluate uncertainties or employ the local polynomial method.

The local polynomial method (Fan and Gubels 1995) involves applying least squares theory to Eq. (3) to optimize the β_i values

$$\left[\hat{\beta}\right] = \begin{bmatrix} \hat{\beta}_0 \\ \hat{\beta}_1 \\ . \\ . \\ . \\ \hat{\beta}_p \end{bmatrix} \tag{4}$$

that minimize Eq. (3), where square brackets denote matrices and "^" denotes an optimized value. This yields Eq. (5)

$$\left[\hat{\beta}\right] = [Z]\,[Y] \tag{5}$$

where

$$[Z] = \left([X]^T \, [W] \, [X] \right)^{-1} [X]^T \, [W] \tag{6}$$

is a 3 x n matrix with entries Z_{ij}. Also, [W] is a diagonal matrix with entries $W_{ii} = G((t - t_i)/h)$, [X] is a matrix with the entries $X_{ij} = (t_i - t)^{j-1}$, and $[Y] = [Y_1, Y_2, \ldots, Y_n]^T$ is a column vector containing the experimental data points. The estimates for the square of the droplet diameter and the instantaneous burning rate $K = -dY/dt = -d(d^2)/dt$ at the time t are thus given by Eqs. (7) and (8).

$$d^2 = \hat{\beta}_0 = \sum_{j=1}^{n} Z_{1j} Y_j \tag{7}$$

$$K = -\hat{\beta}_1 = -\sum_{j=1}^{n} Z_{2j} Y_j \tag{8}$$

The function locpol (Cabrera 2012) in the computer language R (R Core Team 2013), was employed to provide local polynomials for Y as a function of t. Figure 3a shows plots of experimental values of d^2 vs. t for a heptane droplet (Dietrich et al. 2013) as well as the local polynomial fits to the data for h = 0.1, 0.5, and 1 s. Differences between the local polynomial fits and the data are very small over the long time scale shown in Fig. 3a. However, when these same data are viewed over a smaller time scale, differences between the data and the local polynomial fits become apparent (Fig. 3b). These differences are especially relevant when burning rates are estimated from the local polynomial fits, as described below. The "dip" in the data in Fig. 3a at about 23 s is because the droplet partially left the field of view (FOV) for a short time, causing d^2 to artificially decrease until the droplet completely returned to the FOV at about 28 s, when the droplet size increased. The droplet partially left the FOV again at about 33-34 s, after which the data terminate.

Burning rates (K) are evaluated using Eq. (8). As shown in Fig. 4, burning rate histories show less scatter as h is

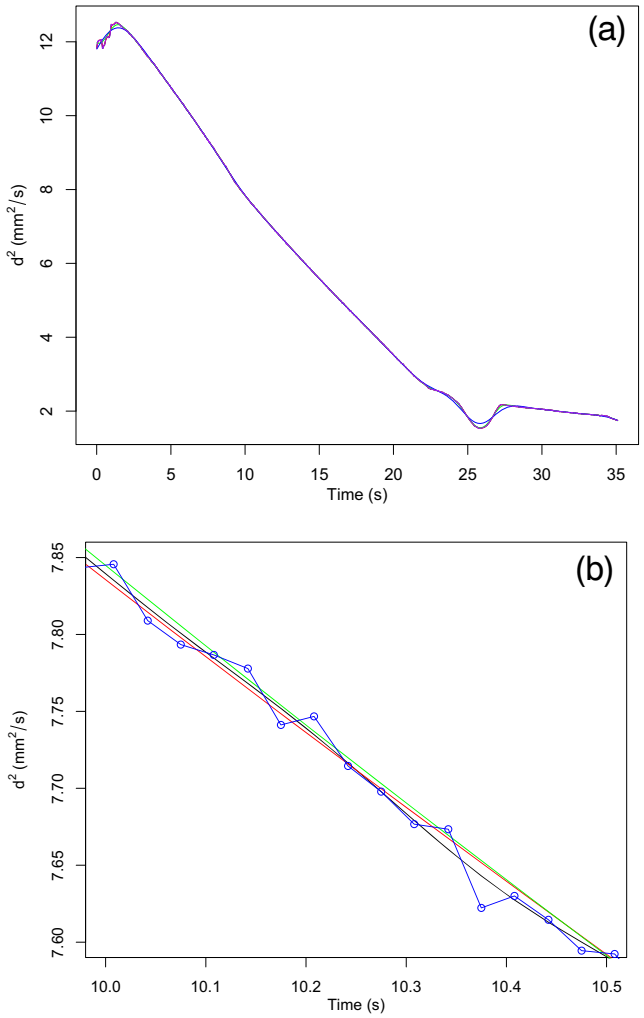

Fig. 3 **a** Droplet size history for a free heptane droplet with local polynomial curve fits; and **b** same data but over a smaller time scale. The experimental data are denoted by circles

increased. The reason for this is that increasing the bandwidth smooths the curve fit (Fig. 3b). Figure 4 suggests that h = 0.5 s and h = 1 s appear to provide reasonably smooth estimates of the burning rate history. The value h = 0.1 s includes short timescale fluctuations in the data, which are likely from noise since rapid fluctuations in K are not expected in the FLEX and FLEX-2 experiments.

Evaluation of Uncertainties

We follow the methodology of the Guide to the Expression of Uncertainty in Measurement (International Organization of Standardization (ISO) 2008) for evaluation of uncertainties. The combined standard uncertainty in the square of the droplet diameter for an image is given by Eq. (9)

$$u_{Y_i} = \left(s_{Y_i}^2 + b_{Y_i}^2\right)^{1/2} \tag{9}$$

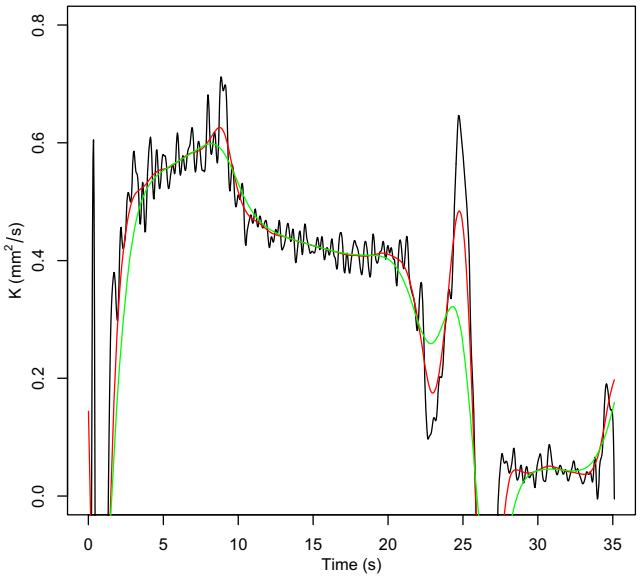

Fig. 4 Burning rate data for a free heptane droplet calculated using local polynomial curve fits: *black line*, h = 0.1 s; *red line*, h = 0.5 s; *green line*, h = 1 s

where s_{Y_i} and b_{Y_i} are the type A and type B standard uncertainties for Y_i, respectively. Following the International Organization of Standardization (ISO) (2008), type A uncertainties are evaluated using statistical analyses while type B uncertainties are estimated using other methods, i.e., by methods other than statistical analysis of a series of observations.

Based on Eq. (2), b_{Y_i} is evaluated as shown in Eq. (10). Equation (10), which estimates Type B standard uncertainties in Y_i, is of the standard form that results when the Taylor series method is employed (International Organization of Standardization (ISO) 2008).

$$b_{Y_i}^2 = \left(\frac{\partial Y_i}{\partial N_{p_i}}\right)^2 b_{N_{p_i}}^2 + \left(\frac{\partial Y_i}{\partial A_p}\right)^2 b_{A_p}^2 + 2\left(\frac{\partial Y_i}{\partial N_{p_i}}\frac{\partial Y_i}{\partial A_p}\right) b_{N_{p_i}A_p} \tag{10}$$

Evaluating the derivatives by differentiating Eq. (2) yields Eq. (11).

$$b_{Y_i}^2 = Y_i^2\left(\frac{b_{N_{p_i}}^2}{N_{p_i}^2} + \frac{b_{A_p}^2}{A_p^2} + 2\frac{b_{N_{p_i}A_p}}{N_{p_i}A_p}\right) \tag{11}$$

The camera pixel elements are nominally square and the average area of an individual pixel is equal to the area of the camera field of view (FOV) divided by the total number of pixels, N, i.e.,

$$A_p = \frac{WH}{N} \tag{12}$$

where W is the width of the FOV and H is the height of the FOV. We use the values W = 30.2 ±0.1 mm (95%) and H = 30.3 ±0.1 mm (95%) that are from Dietrich et al.

(2013). The uncertainties in W and H could arise from pixel nonuniformities as well as calibration and optical errors that lead to apparent pixel nonuniformities. The type B standard uncertainty for pixel areas is evaluated as shown in Eq. (13).

$$b_{A_p}^2 = \left(\frac{\partial A_p}{\partial W}\right)^2 b_W^2 + \left(\frac{\partial A_p}{\partial H}\right)^2 b_H^2 + 2\left(\frac{\partial A_p}{\partial W}\frac{\partial A_p}{\partial H}\right) b_{WH} \tag{13}$$

After evaluating the derivatives by differentiating Eq. (12), Eq. (13) becomes

$$b_{A_p}^2 = \frac{A_p^2}{4}\left(\frac{b_W^2}{W^2} + \frac{b_H^2}{H^2} + 2\frac{b_{WH}}{WH}\right) \tag{14}$$

where we assume that $b_W = U_W/2 = 0.05$ mm and $b_H = U_H/2 = 0.05$ mm. The variables U_W and U_H are the expanded uncertainties for W and H, at a 95% confidence level, respectively. We evaluate the covariance term as $b_{WH} = b_W b_H$ under the assumption that W and H share the same elemental error source (Coleman and Steele 2009), where an elemental error is an error associated with a specific (individual) error source such as the linearity of an instrument used for calibrating a length measurement. Inserting the numerical values for b_W,b_H,W, and H into Eq. (14) yields the following estimate.

$$\frac{b_{A_p}}{A_p} = 0.0033 \tag{15}$$

The variable N_{p_i} will depend on the pixel areas, discretization in spatial coordinates (i.e., finite pixel sizes) as well as discretization of the light levels sensed by the camera. We thus write Eq. (16), which is based upon typical methods of combining standard uncertainties (Coleman and Steele 2009).

$$b_{N_{p_i}}^2 = \left(\frac{\partial N_{p_i}}{\partial A_p}\right)^2 b_{A_p}^2 + b_{sd}^2 + b_{gd}^2 \tag{16}$$

Here, b_{sd} and b_{gd} are the type B standard errors for camera spatial and grayscale discretizations, respectively. If we assume that the number of pixels scales inversely with the average pixel area, then Eq. (17) results.

$$\frac{b_{N_{p_i}}^2}{N_{p_i}^2} = \frac{b_{A_p}^2}{A_p^2} + \frac{b_{sd}^2}{N_{p_i}^2} + \frac{b_{gd}^2}{N_{p_i}^2} \tag{17}$$

We now consider discretization effects, i.e., the effects of finite pixel sizes and finite grayscale discretizations. If the number of pixels comprising the droplet shadow is large, then we may consider variations in the variable φ_i, which we define as the thickness in pixels of a strip that bounds the location of the droplet edge for image i. This variable will be influenced by spatial and grayscale discretizations. The number of pixels, δN_{pi}, comprising a strip of thickness φ_i at the droplet edge is approximately $2\pi^{1/2}\phi_i N_{p_i}^{1/2}$. This can be reasoned by considering the equivalent radius, R_{p_i}, of a circle in "pixel space", where the pixels are uniformly distributed. If the area of an individual pixel is unity, then $N_{p_i} = \pi R_{p_i}^2$ and $\delta N_{p_i} \approx 2\pi R_{p_i}\delta R_{p_i}$. If we set $\delta R_{p_i} = \phi_i$ and note that $R_{p_i} = \left(N_{p_i}/\pi\right)^{1/2}$, then $\delta N_{p_i} \approx 2\pi^{1/2}\phi_i N_{p_i}^{1/2}$. We assume that $\left(b_{sd}^2 + b_{gd}^2\right)^{1/2} \approx \delta N_{p_i}/4$, leading to Eq. (18).

$$b_{sd}^2 + b_{gd}^2 \approx \frac{\pi\phi_i^2 N_{p_i}}{4} \tag{18}$$

Equation (17) can thus be written as follows.

$$\frac{b_{N_{p_i}}^2}{N_{P_i}^2} = \frac{b_{A_p}^2}{A_p^2} + \frac{\pi\phi_i^2}{4N_{p_i}} \tag{19}$$

Finally, we need to evaluate the covariance term $b_{N_{p_i}A_p}/\left(N_{p_i}A_p\right)$ in Eq. (11). We assume that this term includes only elemental errors that are common between N_{p_i} and A_p (Coleman and Steele 2009). In the present context, this involves accounting for influences of pixel area errors on the number of pixels in the droplet shadow. Because N_{p_i} will scale inversely with A_p, we thus model the covariance term as shown in Eq. (20).

$$\frac{b_{N_{p_i}A_p}}{N_{p_i}A_p} = \frac{b_{A_p}^2}{A_p^2} \tag{20}$$

Combining Eqs. (11), (17), and (20) yields Eq. (21).

$$\frac{b_{Y_i}}{Y_i} = \left(4\frac{b_{A_p}^2}{A_p^2} + \frac{\pi\phi_i^2}{4N_{p_i}}\right)^{1/2} \tag{21}$$

The s_{Y_i} terms are evaluated by considering deviations from the local polynomial curve fit as shown in Eq. (22). The derivation of this equation is available in the literature (Fan and Gubels 1995).

$$s_{Y_i}^2 = \frac{\sum_{i=1}^{n}\left[\left(Y_i - \sum_{j=0}^{p}\beta_j\left(t_i - t\right)^j\right)^2 G\left(\frac{t_i - t}{h}\right)\right]}{trace\left\{[W] - [W][X]\left([X]^T[W][X]\right)^{-1}[X]^T[W]\right\}} \tag{22}$$

The combined standard uncertainty in the burning rate is given by Eq. (23).

$$u_K = \left(b_K^2 + s_K^2\right)^{1/2} \tag{23}$$

The variables s_K and b_K are the type A and type B standard uncertainties in K, respectively. If we neglect time uncertainties, i.e., it is assumed that the camera frame rate is

constant, then these standard uncertainties are evaluated as follows.

$$b_K^2 = \sum_{i=1}^{n}\sum_{j=1}^{n}\frac{\partial K}{\partial Y_i}\frac{\partial K}{\partial Y_j}b_{Y_iY_j} \tag{24}$$

$$s_K^2 = \sum_{i=1}^{n}\sum_{j=1}^{n}\frac{\partial K}{\partial Y_i}\frac{\partial K}{\partial Y_j}s_{Y_iY_j} \tag{25}$$

The derivatives in Eqs. (24) and (25) are evaluated by differentiating Eq. (8), yielding Eq. (26).

$$\frac{\partial K}{\partial Y_i} = -Z_{2i} \tag{26}$$

Equations (24) and (25) thus become as follows

$$b_K^2 = \sum_{i=1}^{n}\sum_{j=1}^{n}Z_{2i}Z_{2j}b_{Y_iY_j} \tag{27}$$

$$s_K^2 = \sum_{i=1}^{n}\sum_{j=1}^{n}Z_{2i}Z_{2j}s_{Y_iY_j} \tag{28}$$

where it is recalled that the summations are over all n points in a data set. The covariance terms in Eq. (27) are modeled as $b_{Y_iY_j}^2 = b_{Y_i}b_{Y_j}$ where b_{Y_i} values are evaluated using Eq. (15). Similarly, covariance terms in Eq. (28) are modeled as $s_{Y_iY_j}^2 = s_{Y_i}s_{Y_j}$ where s_{Y_i} values are evaluated using Eq. (22).

An important variable in these analyses is φ_i, which is difficult to characterize for the present data set because edge intensities were manually specified. A realistic lower limit is $\varphi_i = 1$, i.e., it is unlikely that the droplet edge can be determined to within better than one-half of a pixel using manual methods. Estimates suggest that a reasonable practical value is $\varphi_i = 3$, i.e., that the droplet edge can be located to within about ±1.5 pixels. This is based upon the fact that the droplet edge is not sharp in the images but is somewhat diffuse. The thickness of this diffuse region is typically about three pixels, yielding $\varphi_i = 3$ as a practical value.

Figure 5a shows experimental Y data for a methanol droplet (the black line) along with the local polynomial fit (the green line). These two lines, which were determined using h = 0.5 s, are virtually indistinguishable. Figure 5b shows the calculated droplet burning rate history and Figs 5c and 5d show the expanded uncertainties, U_Y and U_K, at a 95% confidence level, respectively, where the black lines correspond to $\varphi_i = 1$ and the red lines $\varphi_i = 3$. The expanded uncertainties are calculated by multiplying the combined standard uncertainties by the coverage factor k = 2 (for a 95% confidence level), i.e., $U_Y = k\,u_Y$ and $U_K = k\,u_K$. These uncertainties show some variations with time. For example, uncertainties in Y are larger near the beginning of the droplet history, which is reasonable as ignition transients may not have decayed to small levels. Uncertainties in Y also show a small temporary increase near about 16 s, which is when this droplet extinguished and the burning rate then decreased substantially. The uncertainties in K are largest near the beginning of the droplet history and also during the extinction period when K changes rapidly with time. Not considering the regions where uncertainties are large, i.e., during the ignition and extinction periods, representative expanded uncertainties for Y and K are $U_Y \approx 0.2$ mm^2 and $U_K \approx 0.005$ mm^2/s, for $\varphi_i = 3$. Because $Y = d^2$, a representative expanded uncertainty in the droplet diameter d is $U_d \approx 0.1$ mm (95%). It is noted that uncertainties in Y are increased by relatively small amounts during an extinction event. As a result, it is reasonable to expect that the droplet diameter at extinction can typically be determined with an uncertainty of about 0.1 mm (95%).

The uncertainty in Y increases as the value of φ_i increases (Fig. 5c), which is reasonable because increasing φ_i means that the location of the droplet edge is known with less certainty. However, increasing φ_i from 1 to 3 has a minimal effect on burning-rate uncertainties (Fig. 5d), which is reasonable if φ_i is held constant, i.e., it does not vary with time when analyzing an entire data set, as was done here. It is noted, however, that U_K can actually decrease slightly as φ_i is increased. This is a result of including covariance terms, which can increase or decrease overall uncertainties, depending on their signs, as has been discussed elsewhere (Coleman and Steele, 2009). In the present analyses it was found that the covariance terms $s_{Y_iY_j}$ influenced burning-rate uncertainties by essentially negligible amounts. This was determined by repeating the calculations both with and without these terms. In contrast, neglecting the covariance terms $b_{Y_iY_j}$ increased burning-rate uncertainties by roughly a factor of 2-3, i.e., accounting for these particular covariances had an appreciable impact on the analysis and in the present case these covariances decreased U_K.

Figures 6 and 7 show analogous data for a heptane droplet and a decane/propylbenzene droplet, respectively. The uncertainties in both cases are largest during and shortly after the ignition period, but after this period the uncertainties are about the same as for the methanol droplet. The early-time uncertainties in the droplet size are larger for the decane/propylbenzene droplet because of strong soot obscuration of the droplet edge, which made it difficult to determine droplet sizes. The soot levels became smaller as time progressed, allowing the droplet edge to be imaged more clearly. This led to the substantially smaller uncertainties that are evident in Fig. 7c after about 2 s. Comparison of the burning-rate uncertainties in Figs. 5d and 6d shows that after early ignition transients, U_K is of the order of 0.005

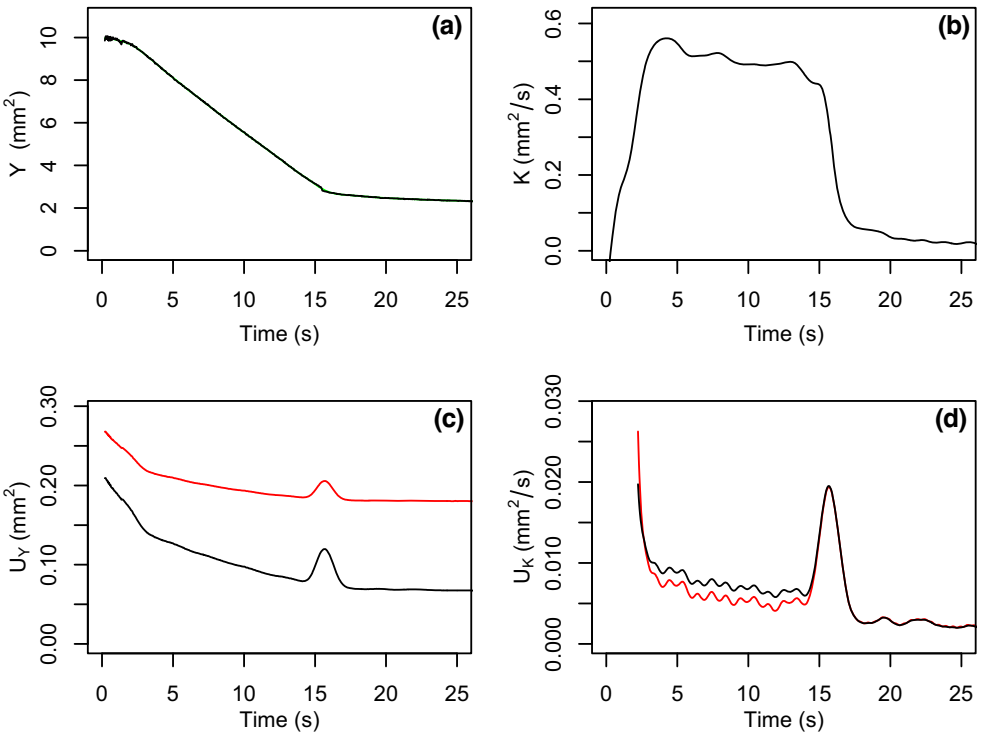

Fig. 5 **a** Experimental Y data (*black line*) and the local polynomial fit (*green line*); **b** burning rate history; **c** 95% uncertainty in Y for $\varphi_i = 1$ (*black line*) and $\varphi_i = 3$ (*red line*); and **d** 95% uncertainty in K for $\varphi_i = 1$ (*black line*) and $\varphi_i = 3$ (*red line*). All calculations were performed with h = 0.5 s for a methanol droplet

mm^2/s for methanol and n-heptane droplets. The corresponding U_K values for a decane/propylbenzene droplet are significantly larger, being about 0.02 mm^2/s. This increased uncertainty is likely a result of the higher sooting levels evident with decane/propylbenzene. The large soot agglomerates that occur when decane/propylbenzene droplets are burned can cause the droplet edge to appear somewhat jagged, as noted by Dembia et al. (2012), which increases the noise in the droplet edge measurements.

The burning-rate uncertainties in Fig. 5d show small oscillations while such oscillations are not evident in Figs. 6d and 7d. This may be a result of the fact that

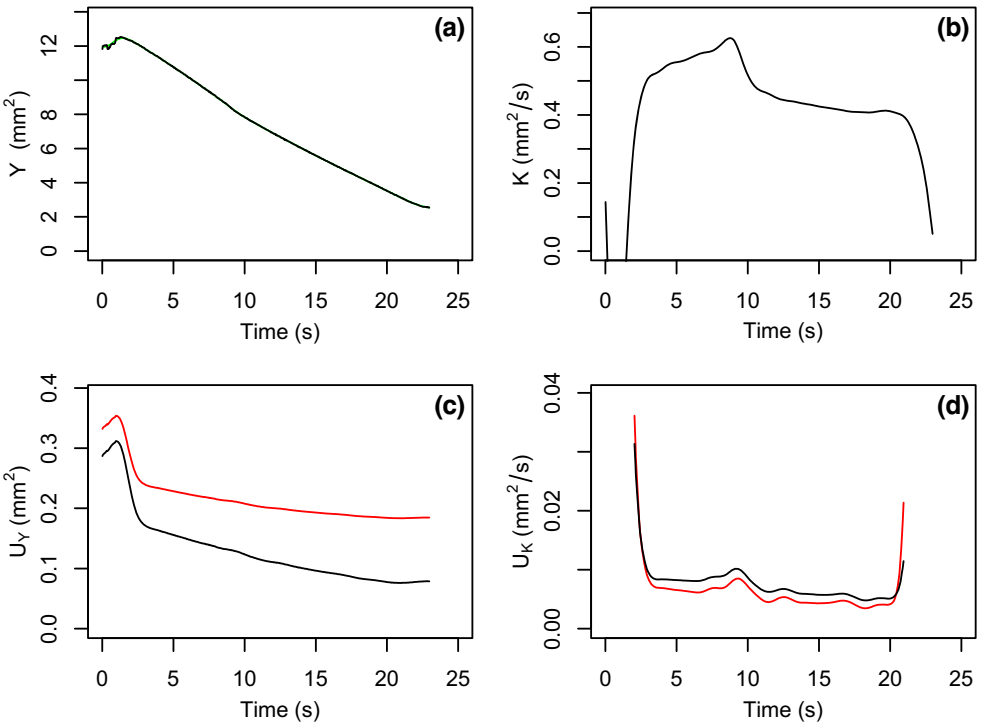

Fig. 6 **a** Experimental Y data (*black line*) and the local polynomial fit (*green line*); **b** burning rate history; **c** 95% uncertainty in Y for $\varphi_i = 1$ (*black line*) and $\varphi_i = 3$ (*red line*); and **d** 95% uncertainty in K for $\varphi_i = 1$ (black line) and $\varphi_i = 3$ (*red line*). All calculations were performed with h = 0.5 s for a heptane droplet

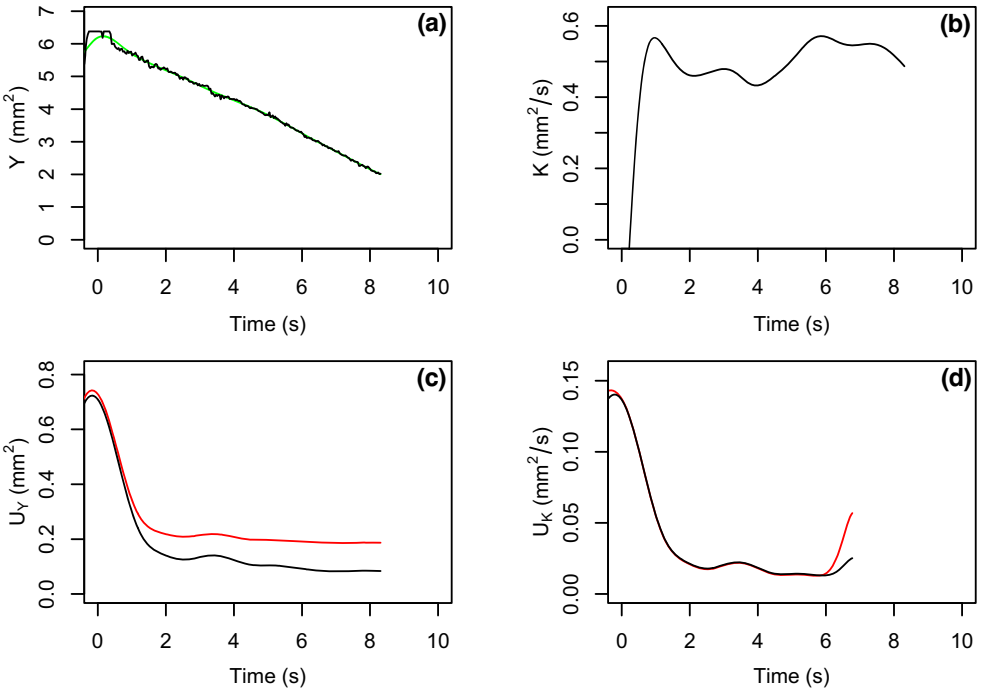

Fig. 7 **a** Experimental Y data (*black line*) and the local polynomial fit (*green line*); **b** burning rate history; **c** 95 % uncertainty in Y for $\varphi_i = 1$ (*black line*) and $\varphi_i = 3$ (*red line*); and **d** 95% uncertainty in K for $\varphi_i = 1$ (*black line*) and $\varphi_i = 3$ (*red line*). All calculations were performed with h = 0.5 s for a decane/propylbenzene droplet

Fig. 5 is for a tethered droplet while Figs. 6 and 7 show data for untethered droplets. The tethered droplet was observed to oscillate slightly back and forth along the fiber axis, which likely added noise to the droplet edge location measurements, e.g., through small variations in droplet shapes. Because K depends upon the time derivative of the square of the droplet diameter, and derivatives amplify noise, this noise would appear in the burning-rate uncertainty U_K.

It is noted that the local polynomial method can provide reasonable estimates of instantaneous burning rates, i.e., the entire burning rate history can be evaluated rather than simply finding the slopes of straight lines that are fit to subsets of the data. For example, Fig. 8 shows best-fit straight lines for two portions of the Y-t history for a burning heptane droplet. This is the same droplet also described by Fig. 6. The best-fit lines give burning-rates of about 0.57 mm^2/s and 0.43 mm^2/s. The correlation coefficients are very close

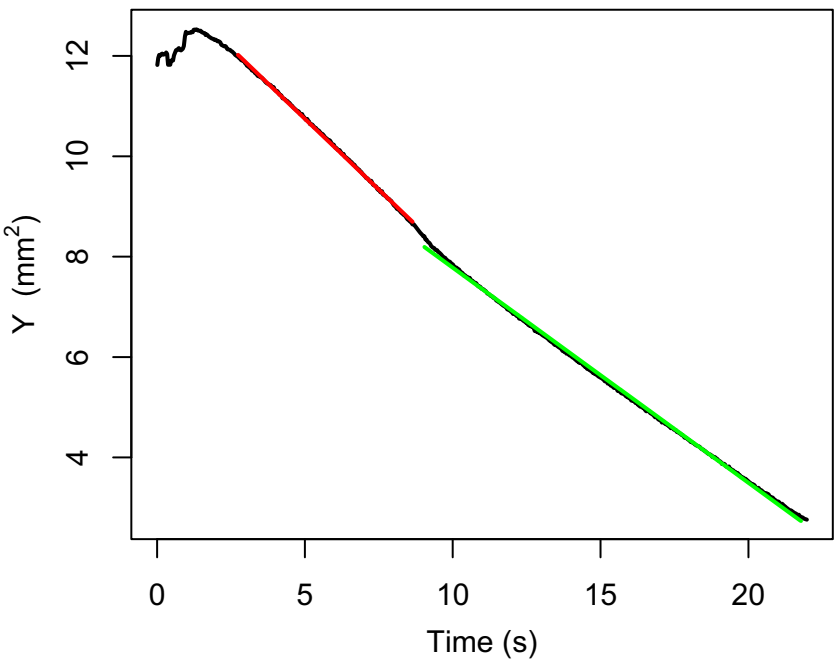

Fig. 8 Experimental Y data and best-fit straight lines for a heptane droplet. *Black*: experimental data. *Red*: best fit with K = 0.564 mm^2/s, $R^2 = 0.99941$. *Green*: best fit with K = 0.429 mm^2/s, $R^2 = 0.99901$

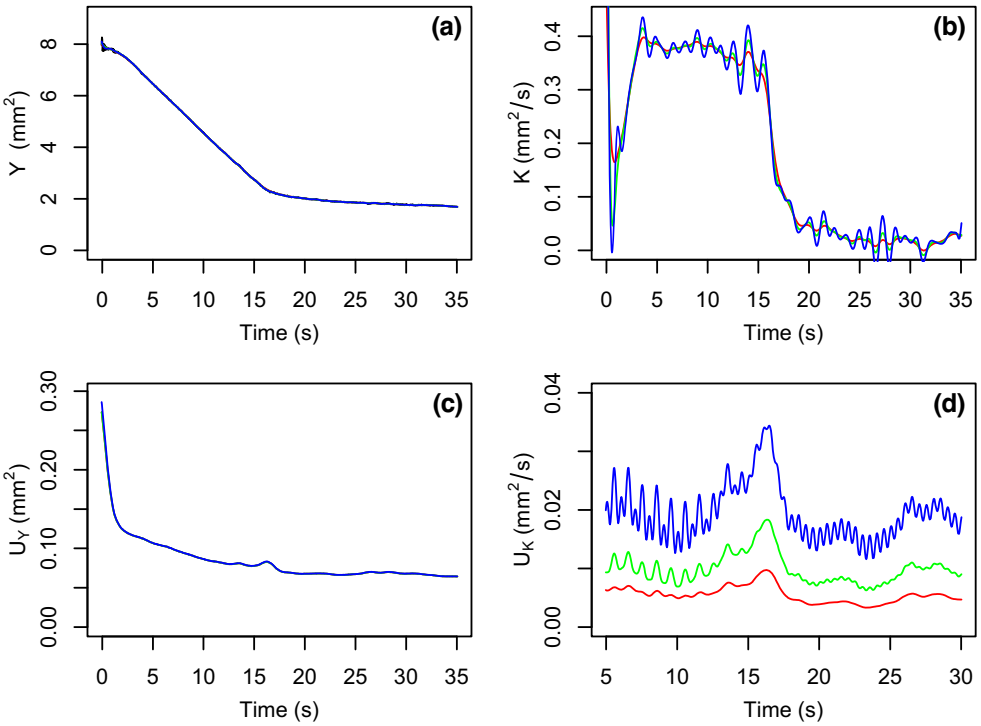

Fig. 9 **a** Experimental Y data (*black line*) and local polynomial fits; **b** burning rate histories; **c** 95% uncertainties in Y for $\varphi_i = 1$; and **d** 95% uncertainties in K for $\varphi_i = 1$. Polynomial orders are p = 2 (*red line*), p = 4 (*green line*), and p = 8 (*blue line*). All calculations were performed with h = 0.5 s for a methanol droplet

to unity in both cases, suggesting that the straight-line fits are excellent. However, Fig. 6b shows that the burning rates are never actually constant. For example, the burning rate during the first time period (3-8 s) varies from about 0.52 mm^2/s to about 0.63 mm^2/s, i.e., the burning rate increases by about 21% over this time period. The arithmetic average of these two burning rates is 0.58 mm^2/s, which is very close to the burning rate obtained with a best-fit straight line.

Finally, it is worth considering the impact of the order of the polynomial, p, used in the local polynomial analyses. Figures 9 and 10 show plots that were obtained for a heptane droplet and a decane/propylbenzene droplet, respectively,

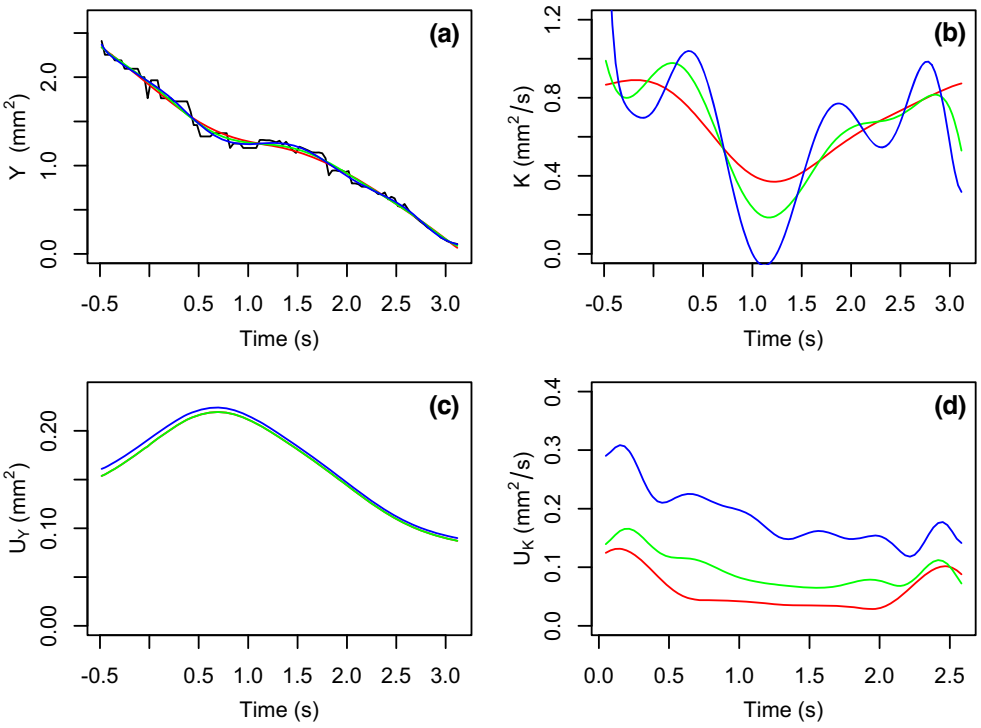

Fig. 10 **a** Experimental Y data (*black line*) and local polynomial fits; **b** burning rate histories; **c** 95% uncertainties in Y for $\varphi_i = 1$; and **d** 95% uncertainties in K for $\varphi_i = 1$. Polynomial orders are p = 2 (*red line*), p = 4 (*green line*), and p = 8 (*blue line*). All calculations were performed with h = 0.5 s for a decane/propylbenzene droplet

for polynomial orders p = 2, 4, and 8. The order of the polynomial has very little influence on the droplet size fits (Figs. 9a and 10a) and the droplet size uncertainties (Figs. 9c and 10c). It is also noted that the results for p = 1 and p = 2 were generally similar, so we do not present results for p = 1, though it is noted that second-order polynomials were better able to model Y data during time periods where burning rates were changing rapidly such as during extinction events than first-order polynomials. Increasing the order of the polynomial to p = 4 or 8 leads to greater variations in the calculated burning rates (Figs. 9b and 10b) and the burning-rate uncertainties increase as p is increased (Figs. 9d and 10d). Higher-order polynomials exhibit more local variations and increased uncertainty levels because they capture more of the noise, which is especially evident for the data in Fig. 10, which are noisier than for Fig. 9. It is for these reasons that the polynomial order p = 2 was used in the present analyses.

Conclusions

Uncertainties in droplet size measurements and burning rates were quantitatively evaluated for droplet combustion experiments that have been performed on the International Space Station. The analyses considered non-sooting methanol or lightly sooting heptane droplets as well as moderately sooting decane/propylbenzene droplets. Type A and type B errors were considered and propagated into the uncertainties via the Taylor series method. It was found that soot can contribute significantly to the droplet size and burning-rate uncertainties.

It is of interest to extend this research so that the uncertainties identified here can be reduced. For example, there may be more optimal image analysis techniques that can be employed for droplet sizing. It would also be worthwhile to perform similar analyses for flame diameters, which can have larger uncertainty levels because of the diffuse nature of the flame. The general procedures used here for droplet size measurements should also be applicable to flame and soot shell measurements. Finally, the uncertainties associated with measurements of droplet diameters for strongly sooting fuels should be reduced, as large amounts of soot can lead to significant background noise by reducing the overall background light intensity as well as by causing the droplet edge to appear to be irregular.

Acknowledgments The financial support of the National Aeronautics and Space Administration is gratefully acknowledged. The Technical Monitor was Dr. Daniel L. Dietrich. We appreciate discussions with V. Berg, D. L. Dietrich, F. L. Dryer, P. Ferkul, M. Hicks, V. Nayagam, and F. A. Williams. We also express our sincere gratitude to the management, engineering, and operations teams at NASA and Zin Technology, Inc. and the ISS astronauts who participated in the experiments. Gratitude is also expressed to A. Austin, H. Daqqa, and R. Wong for their efforts with statistical analysis of the data via the STA 401 class at UC Davis.

References

Cabrera, J.L.O.: locpol: Kernel local polynomial regression. R package version 0.6-0. http://CRAN.R-project.org/package=locpol (2012)

Coleman, H.W., Steele, W.G.: Experimentation, Validation, and Uncertainty Analysis for Engineers. John Wiley, New York (2009)

Dembia, C.L., Liu, Y.-C., Avedisian, C.T.: Automated data analysis for consecutive images from droplet combustion experiments. Image Anal. & Stereology **31**, 137–148 (2012)

Dietrich, D.L., Ferkul, P.V., Bryg, V.M., Nayagam, V., Hicks, M.C., Williams, F.A., Dryer, F.L., Shaw, B.D., Choi, M.Y., Avedisian, C.T.: Detailed Results from the Flame Extinguishment Experiment (FLEX) - March 2009 to December 2010, NASA/TP-2013-216046. NASA John H. Glenn Research Center, Cleveland (2013)

Fan, J.-Q., Gubels, I.: Data driven bandwidth selection in local polynomial fitting: variable bandwidth and spatial adaptation. J. R. Stat. Soc. B **57**, 371–394 (1995)

Farouk, T.I., Dryer, F.L.: On the extinction characteristics of alcohol droplet combustion under microgravity conditions - a numerical study. Combust. Flame **159**, 3208–3223 (2012)

Farouk, T.I., Liu, Y.C., Avedisian, C.T., Dryer, F.L.: Sub-millimeter sized methyl butanoate droplet combustion: Microgravity experiments and detailed numerical modeling. Proc. Comb. Inst. **34**, 1609–1616 (2013)

International Organization of Standardization (ISO): Evaluation of measurement data – Guide to the expression of uncertainty in measurement, JCGM 100:2008 (2008). http://www.bipm.org/utils/common/documents/jcgm/JCGM_100_2008_E.pdf

Law, C.K.: Asymptotic theory for ignition and extinction in droplet burning. Combust. Flame **24**, 89–98 (1975)

Law, C.K.: Combustion Physics. Cambridge University Press, New York (2006)

Liu, Y.C., Farouk, T.I., Savas, A.J., Dryer, F.L., Avedisian, C.T.: On the spherically symmetrical combustion of methyl decanoate droplets and comparisons with detailed numerical modeling. Combust. Flame **160**, 641–655 (2013)

Marchese, J., Dryer, F.L.: The effect of non-luminous thermal radiation in microgravity droplet combustion. Combust. Sci. Technol. **124**, 371–402 (1997)

R Core Team: R: A language and environment for statistical computing. R Foundation for Statistical Computing, Vienna, Austria (2013). http://www.R-project.org/

Sirignano, W.A., 2nd edn Fluid Dynamics and Transport of Droplets and Sprays. Cambridge University Press, New York (2010)

Webster, J.G.: The Measurement Instrumentation and Sensors Handbook. CRC Press, Boca Raton (1999)

Williams, F.A.: Combustion Theory - the Fundamental Theory of Chemically Reacting Flow Systems, Perseus Books, Reading, MA (1985)

Zhang, B.L., Card, J.M., Williams, F.A.: Application of rate-ratio asymptotics to the prediction of extinction for methanol droplet combustion. Combust. Flame **105**, 267–290 (1996)